Electronic Supplementary Material (ESI) for Materials Horizons.

Supporting Information

Defect-suppressed submillimeter-scale WS_2 single crystals with high photoluminescence quantum yield by alternate-growth-etching CVD

Xing Xin, Yanmei Zhang, Jiamei Chen, Mao-Lin Chen, Wei Xin, Mengfan Ding, Youzhe Bao, Weizhen Liu,* Haiyang Xu* and Yichun Liu

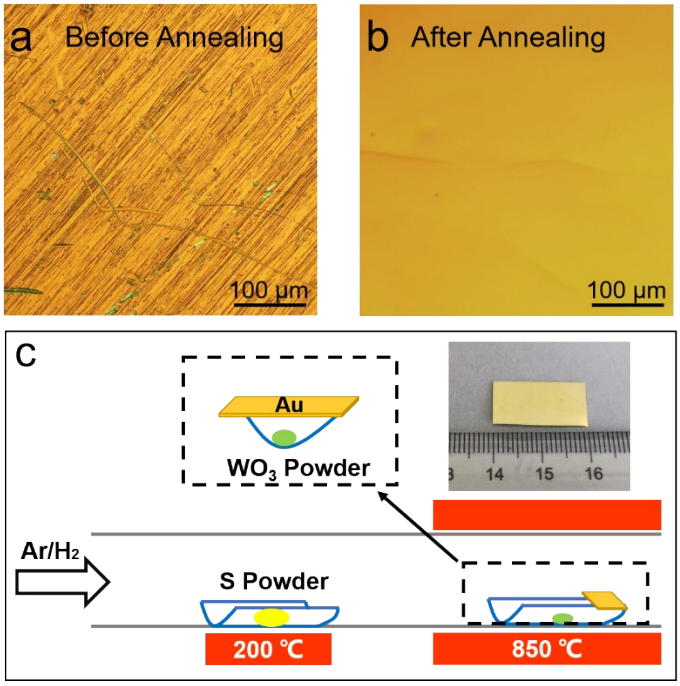

Figure S1. Optical images of a Au foil (a) without long-time annealing and (b) with annealing at 1050 ℃ for more than 12 hours. After annealing the Au foils for 12 hours, the surface becomes smooth and clean, which is beneficial for the growth of large-scale WS_2 single crystals. The annealing treatment is only needed for those Au foils which is used for the first time. (c) Schematic diagram of the synthesis of millimeter-scale monolayer WS_2 single crystals

on Au foils by AGE-CVD. S powder was located outside the high-temperature zone and heated separately. Au is not only a substrate for the deposition of WS_2, but also can lower the barrier energy for the sulfurization of WO_3. The extremely low solubility of W in Au suppressed the formation of WS_2 multilayers, which is beneficial for the surface-catalytic growth of uniform monolayer WS_2.

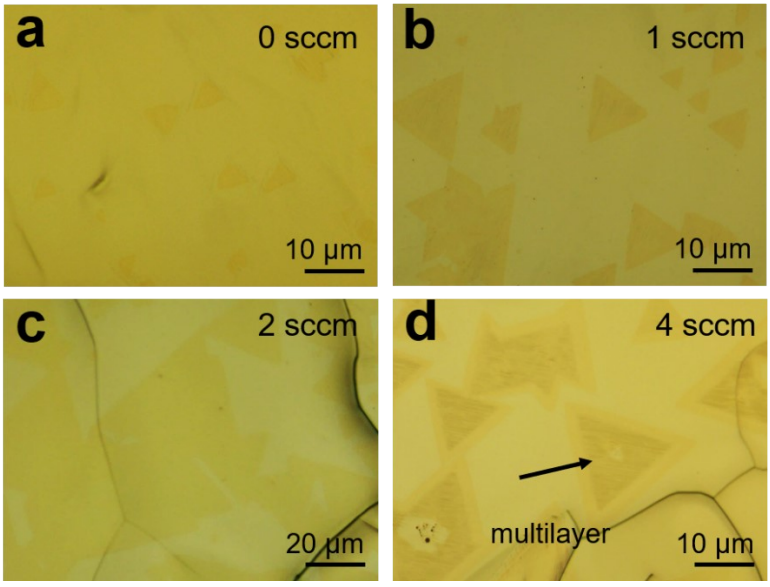

Figure S2. Optical images of WS_2 grown on Au foils with different H_2 flow rate of (a) 0 sccm, (b) 1 sccm, (c) 2 sccm and (d) 4 sccm. Except for changing the H_2 flow rate, we keep all the other CVD parameters constant to eliminate the uncertain factors. Ar flow rate is 100 sccm and the growth time for all samples is 3 min. The grain size of monolayer WS_2 increases along with the H_2 flow rate increasing from 0 to 2 sccm. WS_2 multilayers formed when a higher H_2 flow rate was used.

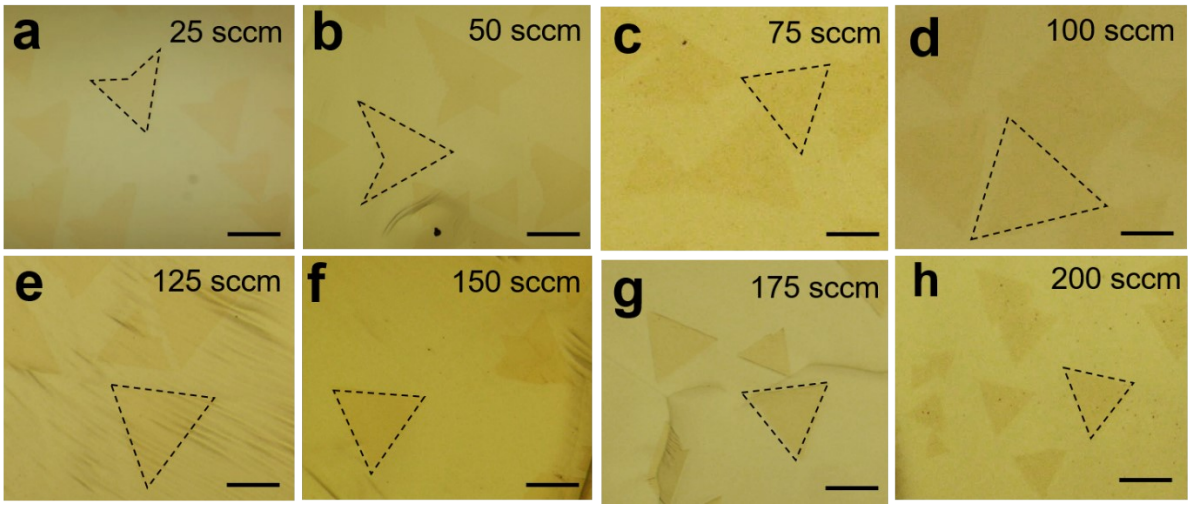

Figure S3. Representative morphologies of WS_2 grown on Au foils with increasing the Ar flow rate of (a) 25 sccm, (b) 50 sccm, (c) 75 sccm, (d) 100 sccm, (e) 125 sccm, (f) 150 sccm, (g) 175 sccm, (h) 200 sccm, respectively. Except for changing the Ar flow rate, we keep all the other CVD parameters constant to eliminate the uncertain factors. H_2 flow rate is 2 sccm and growth time is 3 min. The scale bar in all images is 20 μm. The grain size is defined as the edge length of triangle domains. The grain count in Figure 1a, which reflects the nucleation density, is the number of WS_2 grains in the same area as shown in Figure S3.

The grain size of WS_2 increases with the Ar flow rate from 25 to 100 sccm. Then the grain size and nucleation density of WS_2 decreases with the Ar flow rate from 100 to 150 sccm. The maximum grain size and minimum nucleation density were obtained with an Ar flow of 100 and 150 sccm, respectively. When the Ar flow rate is higher than 150 sccm, nucleation density increases because excess growth sources introduced with carrier gas will increase nucleation sites on Au surfaces.

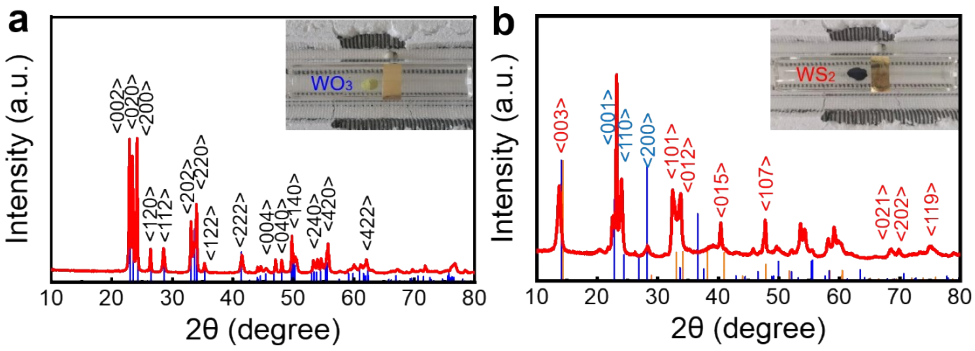

Figure S4. X-ray diffraction (XRD) patterns of WO_3 powders before (a) and after (b) introducing S powders. The crystal facets of WO_3 and WS_2 are colored in blue and red, respectively. After a part of WO_3 powders was sulfurized, the color changed from yellow to black. Both the diffraction peaks of WO_3 and WS_2 exist in the XRD patterns, illustrating that a part of S powders reacted with WO_3 powder at upstream and makes the WO_3 sulfurized in the quartz boat.

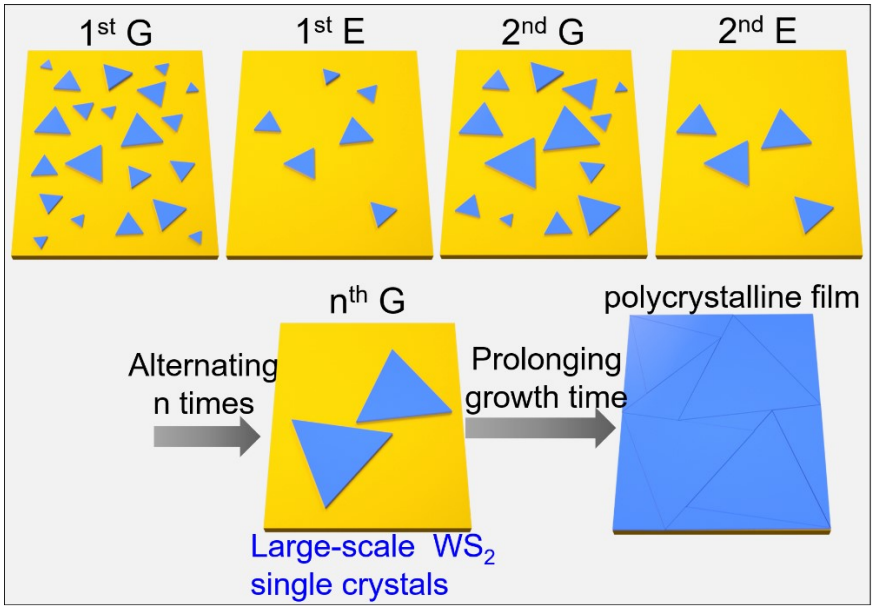

Figure S5. Schematic of alternating the growth and etching stage. AGE-CVD can decrease the nucleation density of WS_2 single crystals, so that we can get a large WS_2 single-crystal with a submillimeter-scale size by repeating the growth and etching for n times (the penultimate picture marked by "n^{th} G" in Fig. S5). The last picture in Fig. S5 is used to show that when the

individual single-crystal WS_2 flake connects with each other by extending the growth time, a continuous polycrystalline WS_2 film will be formed. At this moment, we can't obtain a larger WS_2 single crystal any more.

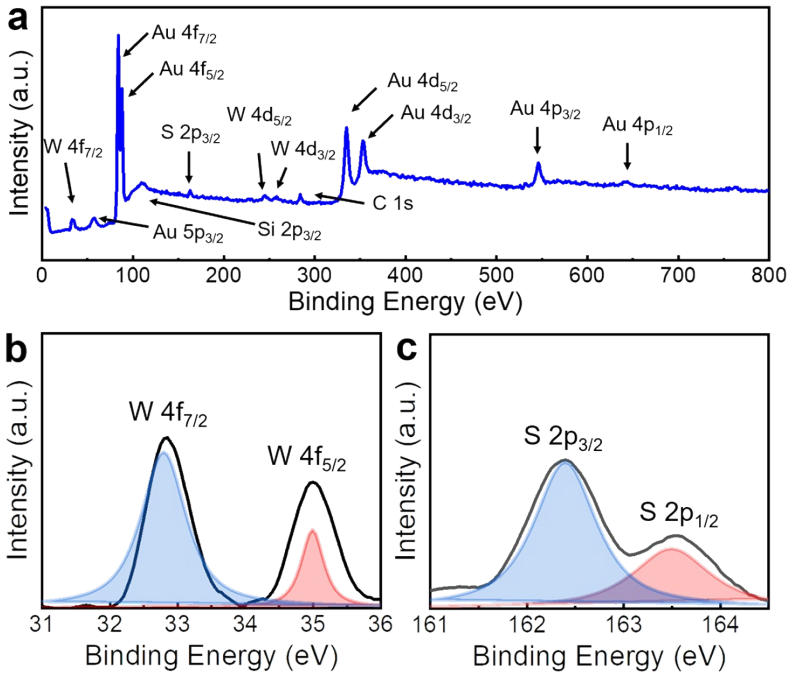

Figure S6. (a) XPS spectra of elemental variation taken on the Au foil after WS_2 growth. The spectra without W-Au alloy signals illustrating the weak interaction between WS_2 and Au. (b) W 4f and (c) S 2p XPS spectra of WS_2 grown on the Au foil, representing the formation of WS_2 on Au foils.

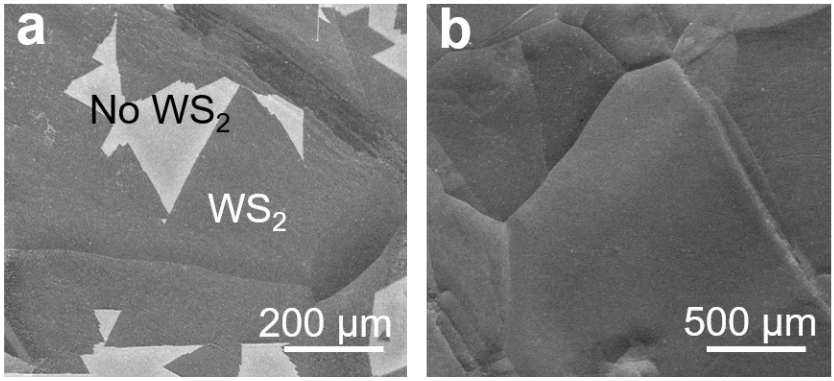

Figure S7. The SEM images of (a) single crystal and (b) continuous films of WS_2, showing that individual WS_2 domains can connect with each other and form a continuous WS_2 film with

further prolonging the growth time of the 5th G to (a) 20 min and (b) 25 min. The white arrow in (b) shows the naked Au area without WS_2. (c)

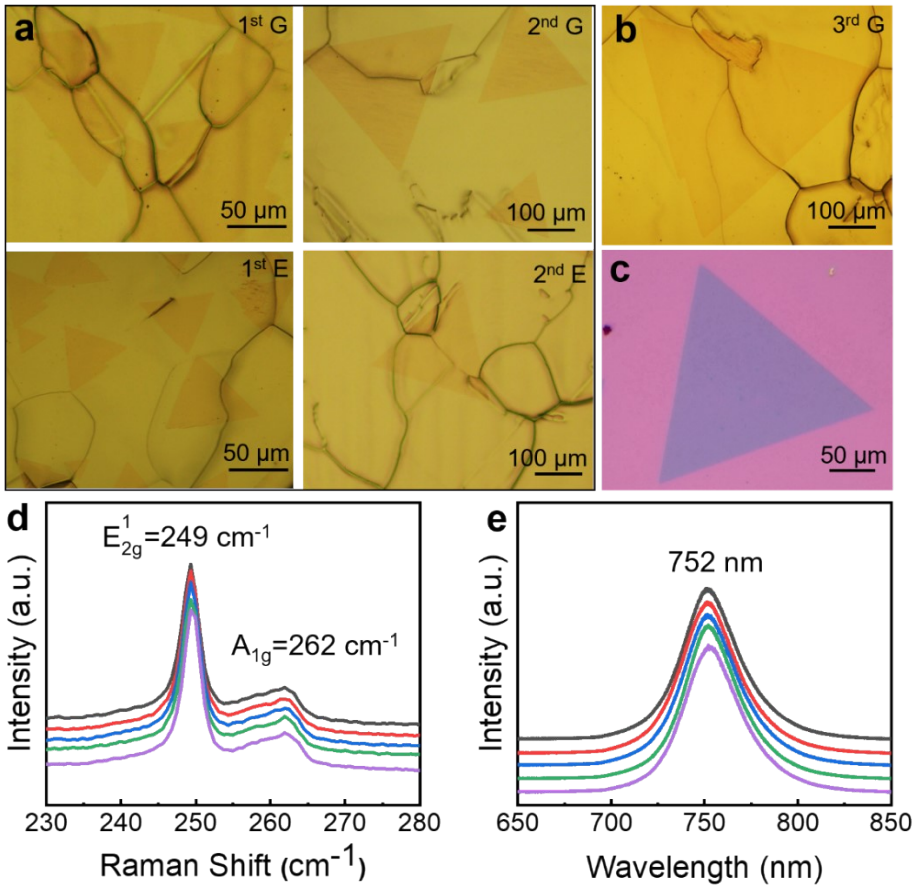

Figure S8. (a-b) A series of optical images of WSe_2 domains grown by AGE-CVD. (c) The optical image of as-grown WSe_2 domain transferred to the SiO_2/Si substrate by electrochemical bubbling method. (d) Raman and (e) PL spectra taken from the different locations of single-crystal WSe_2 domain in (c).

The synthesis of large-scale single-crystal WSe_2 by AGE-CVD:

We also used AGE-CVD to synthesize large-scale high-quality monolayer single-crystal WSe_2 on Au foils. Singe-crystal WSe_2 domains were obtained on Au foils by the same method with changing the growth precursors. The 200 mg Se powder (99.5 wt%) was separately heated to ~350 ℃ at the upstream of the Au foil outside the high temperature zone. The tube furnace

was heated from room temperature to 700 ℃ within 20 min and then to 900 ℃ in 10 min under an Ar flow of 100 sccm. Then after, 5 sccm H_2 was turned on. Large-scale WSe_2 domains with a grain size larger than 500 μm can be obtained after the second cycle.

Figure S8a and b shows that a 500-μm WSe_2 domain was formed at the third growth stage. Similarly, large-scale WSe_2 domain can be completely transferred onto the SiO_2/Si substrates by electrochemical bubbling transfer method (Figure S8c). The representative Raman E^1_{2g} and A_{1g} mode in Figure S8d is located at ~ 249 and 262 cm^{-1}. The PL spectra in Figure S8e shows a single excitonic A peak at ~752 nm, a characteristic of direct bandgap semiconductor. The Raman and PL spectra taken from the different positions in the WSe_2 domain shows the similar shape, indicates the triangle is uniform monolayer.

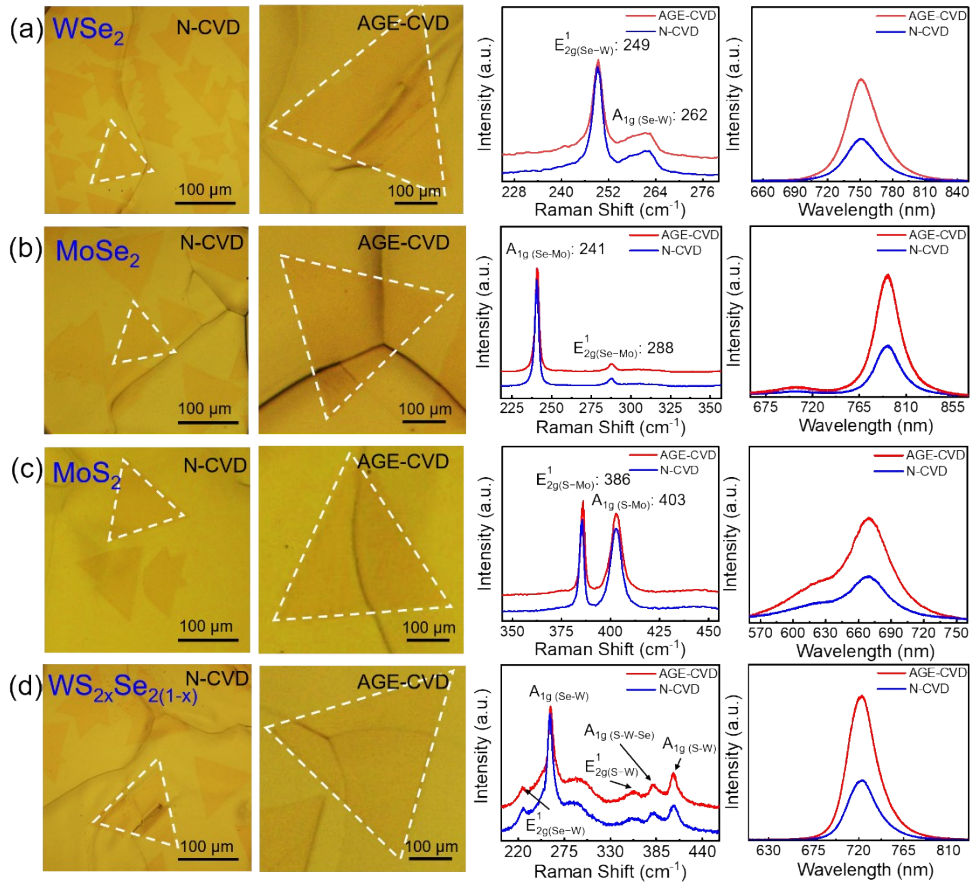

Figure S9. (a) WSe_2, (b) $MoSe_2$, (c) MoS_2 and (d) $WS_{2x}Se_{2(1-x)}$ samples were obtained by N-

CVD and AGE-CVD, respectively. The corresponding Raman and PL spectra were also presented. Except for WS_2 we mainly discussed, these four kinds of TMDs obtain by AGE-CVD also have larger grain sizes and higher PL intensity. These results can fully demonstrate the great advantage and the universality of our AGE-CVD method for the synthesis of high-quality large-scale single-crystal TMDs.

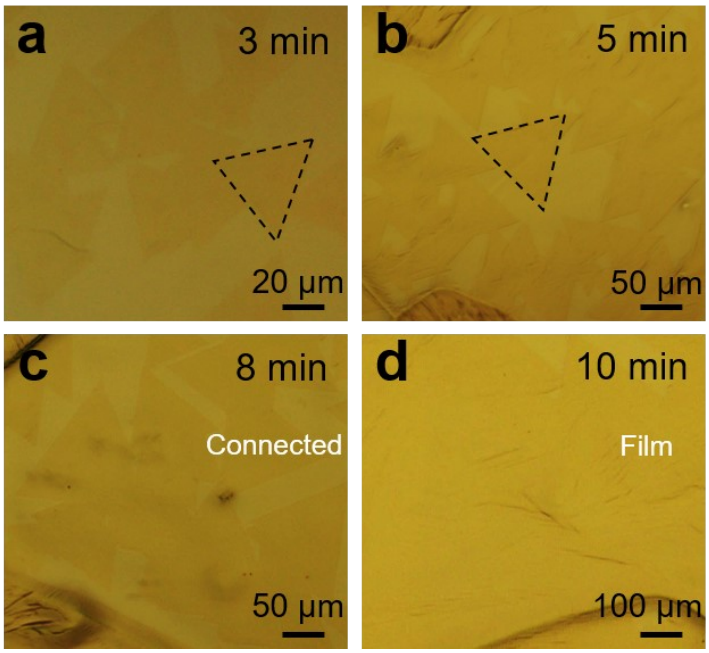

Figure S10. A series of optical images of WS_2 grown by normal CVD. The growth time for (a-d) increased from 3 to 10 min. All the CVD parameters are the same as mentioned in Figure 2. Ar flow rate was 100 sccm during the whole processes. Figure S10b shows that the grain size of individual WS_2 domain is smaller than 120 μm. WS_2 domains were easily connected with each other and finally formed a continuous film. Compared with the results in Figure 2, we can confirm the great advantages of our AGE-CVD in realizing the synthesis of submillimeter-scale WS_2 single crystals. AGE-CVD can dramatically decreased the nucleation density of WS_2 and increased the grain size for 4~5 times larger than N-CVD.

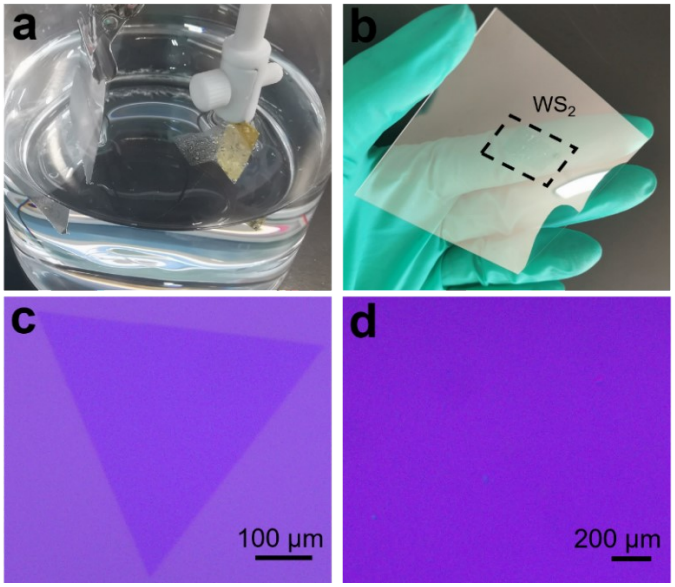

Figure S11. (a) Electrochemical bubbling transfer process and (b) PMMA/WS_2 films with a full coverage in 2 cm^2 transferred onto the transparent PET substrate. (c) Optical images of a submillimeter-scale single-crystal monolayer WS_2 flake with a size of ~520 μm and (d) a uniform polycrystalline WS_2 film on SiO_2/Si substrates after electrochemical bubbling transfer.

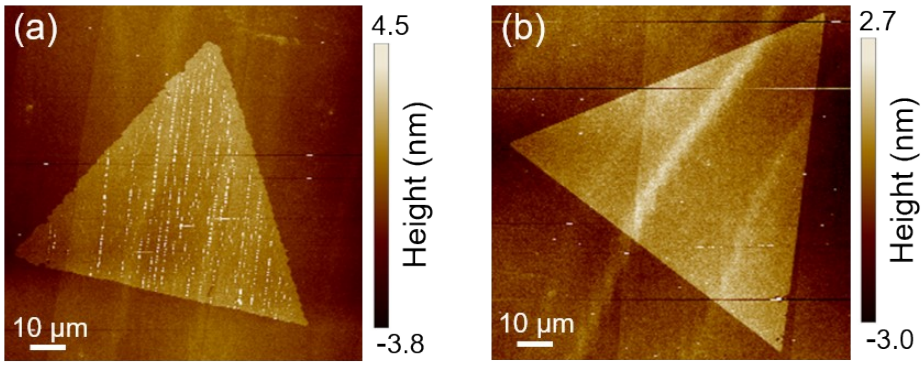

Figure S12. AFM images showing the transfer results by (a) wet etching method and (b) electrochemical bubbling method. There exist many wrinkles and some cracks in WS_2 flake in (a). On the contrary, the WS_2 single crystal transferred by the latter method are very uniform without any obvious wrinkle or void. To be sure, AFM is only applicable to directly scan the whole sample with a size smaller than 100 μm, due to the equipment limitations.

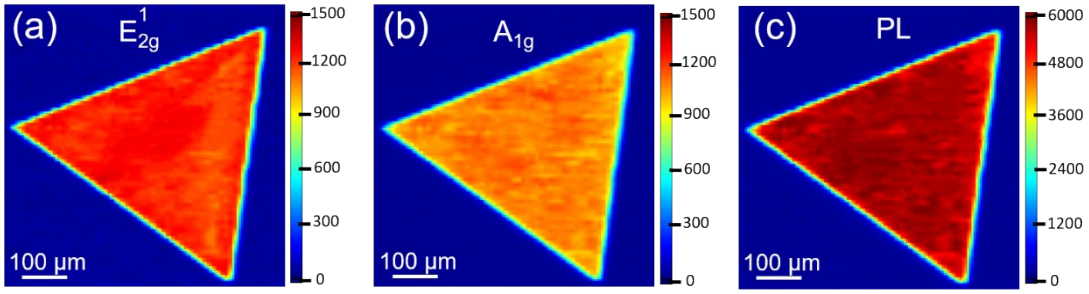

Figure S13. The intensity mappings of (a) E^1_{2g} (356 cm^{-1}), (b) A_{1g} (418 cm^{-1}) and (c) PL peak (613 nm) of a WS_2 single crystal with a grain size of ~520 μm detected on a SiO_2/Si substrate.

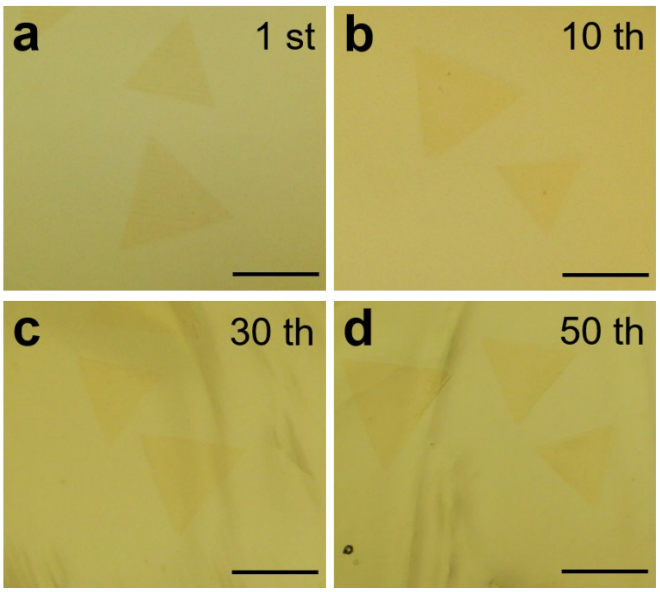

Figure S14. WS_2 single crystals grown on the same reusable Au foils for (a) the first time, (b) 10 times, (c) 30 times and (d) 50 times, respectively. All the triangle WS_2 domains were obtained at the 3rd E stage as mentioned in Figure 2 and they show the similar morphology. The scale bar in all images is 100 μm.

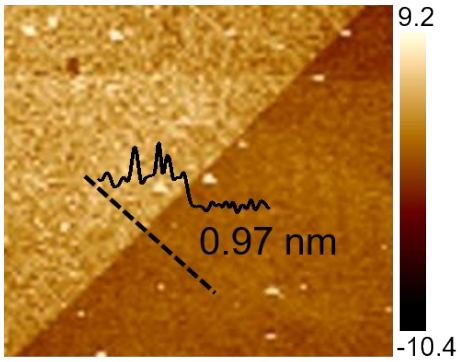

Figure S15. AFM height topography detected at the edge of single-crystal WS_2. The height profile in the inset shows thickness of WS_2 is ~0.97 nm, which was measured along the black dotted line.

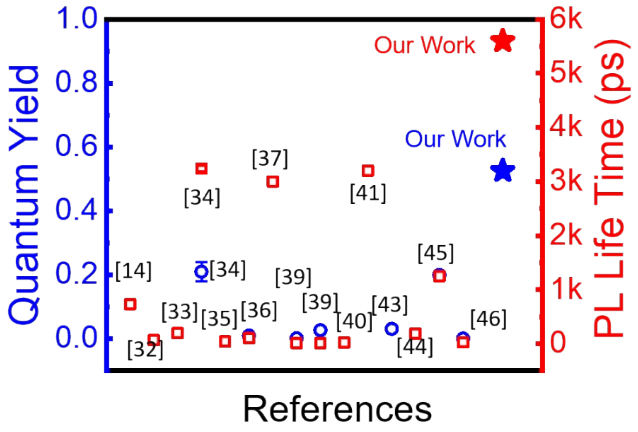

Figure S16. Comparison of PL performance between our WS_2 and reported TMDs in the literatures. The corresponding references are listed in Table S2 below.

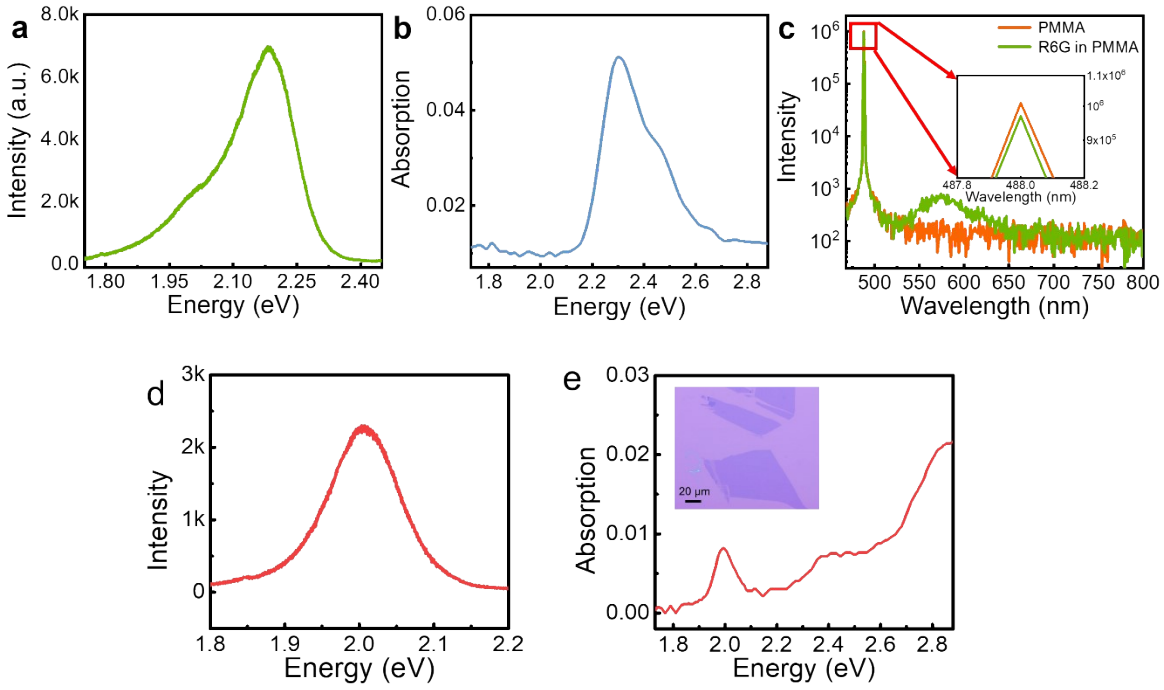

Figure S17. (a) PL spectra and (b) UV-vis absorption spectrum of R6G film. The wavelength of excitation laser was 488 nm, which is the same as the laser used for WS_2 in Figure 5. (c) PL spectra of the PMMA films with (green curve) and without (orange curve) R6G molecules measured by an integrating sphere. Inset shows the enlarged linear portion of the spectra. (d) PL spectra and (e) UV-vis absorption spectrum of mechanically-exfoliated WS_2 measured under the same experimental conditions. The inset in (e) shows the WS_2 monolayer samples obtained via mechanical exfoliation of a bulk crystal. It was measured under the same experimental conditions as shown in Fig.5.

PL QY measurements of R6G.

The PL QY of WS_2 was measure with Rhodamine 6G (R6G) as reference, because it has outstanding chemical stability, high QY and no overlap between absorption and emission spectra. R6G is dispersed uniformly into a poly(methyl methacrylate) (PMMA) solution as solvent by the Roy's method.[46] The reference R6G film was spin-coated onto sapphire. Figure

S17 (a and b) show the PL emission and absorption of the R6G reference film. PMMA with and without R6G films were then loaded into an integrating sphere with a 488 nm laser. Corresponding PL spectra are illustrated in Figure S17c. The QY of R6G is estimated by the equation:

$$Q_R = \frac{I_e}{I_a} \quad (1)$$

Here, I_e is the emission of R6G, the difference of integrated intensity of PL spectra at ~560 nm from PMMA with and without R6G. I_a is the absorption of R6G, the reduction of the PL peak intensity at 488 nm from PMMA without and with R6G. The measured QY of R6G (Q_R) is calculated to be ~53.5%.

PL QY of mechanically-exfoliated WS_2

By measuring the PL emission intensity and UV-vis absorption of mechanically-exfoliated WS_2 (Figure S17d and e) and R6G (Figure S17a and b) with the same excitation laser (488 nm). PL QY of WS_2 (QW) is calculated to be ~25.5% by using the same equation in Figure 5.

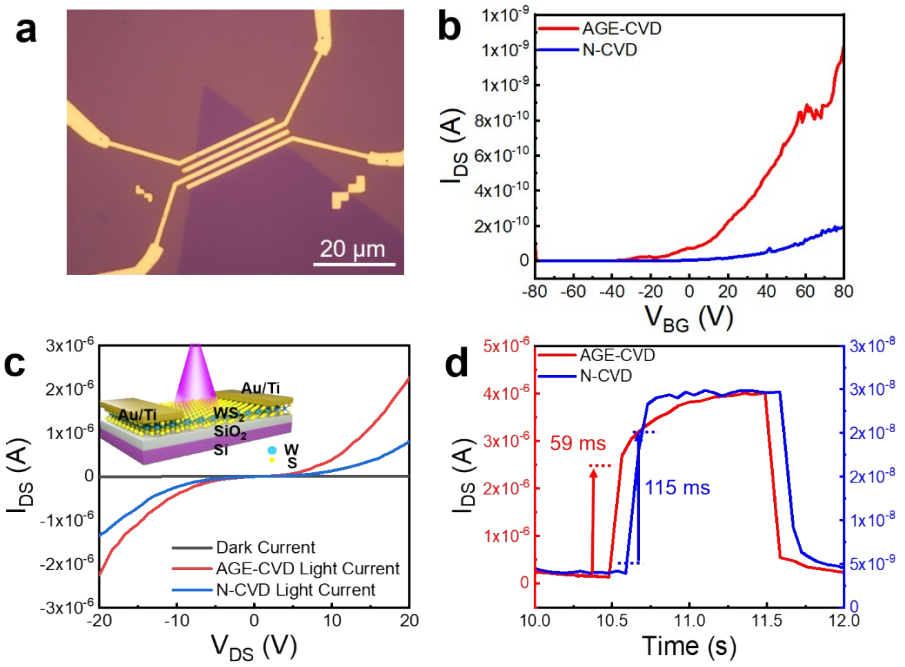

Figure S18. Electrical properties characterization of monolayer single-crystal WS_2 grown by AGE and N-CVD. (a) Optical image of the back-gate field effect transistor (FET) device based on the single-crystal WS_2 domain. (b) Transfer characteristic of WS_2 FET devices fabricated with WS_2 grown by AGE and N-CVD. All the measurements were taken under ambient pressure at room temperature. V_{ds} is 0.1 V in (b). The carrier mobility (μ) and ON/OFF ratio of WS_2 domains obtained by AGE and N-CVD is 8.3 and 0.56 $cm^2\ V^{-1}\ s^{-1}$, $\sim 10^3$ and 3×10^2, respectively. (c) Transfer curves of the photodetectors tested in air with and without light illumination. The inset is the schematic diagram of photodetector. V_{ds} is 20 V and the light illumination power is 0.1 mW with a wavelength of 405 nm. The responsivity (R) is 22.9 and 13.8 mA W^{-1} for WS_2 domains obtained by AGE and N-CVD. (d) Magnified part of the time-dependent source-drain current with switch ON/OFF laser pulse.

FET fabrication and electrical property measurements.

Monolayer single-crystal WS_2 domains were transferred onto highly doped Si substrates, then a 5 nm Ti/50 nm Au layer was deposited by electron beam evaporation as source and drain electrodes. The channel width and length of the FET device were 0.6 and 25 μm, respectively. Electrical properties of FET were measured under ambient conditions at room temperature using an Agilent semiconductor parameter analyzer (4155C Semiconductor Parameter Analyzer). The field mobility was determined by the following equal:

$$\mu = \left(\frac{L}{WC_{OX}V_d}\right)\left(\frac{\Delta I_d}{\Delta V_g}\right) \quad (2)$$

Where L and W represent channel width and length, respectively, and C_{ox} is the capacitance of the dielectric layer (300-nm thick SiO_2).

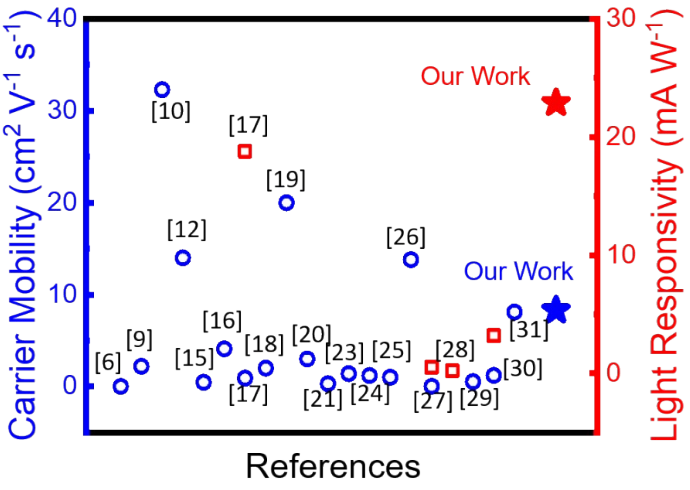

Figure S19. Comparison of electrical properties between our WS_2 and reported CVD-grown WS_2 in the literatures. The corresponding references are listed in Table S1 below. Although the carrier mobility (8.3 cm^2 V^{-1} s^{-1}) and light responsivity (22.9 mA W^{-1}) detected based on a FET device are not the highest values among these reported results in Table S1, they are still at relatively high levels. The possible reason is that the intrinsic electronic properties of WS_2 may be affected by the complex device fabricating processes. We will further optimize the device fabricating process (e.g. electrode contact and device structure design) in our future work to obtain better electrical properties.

Table S1. Comparison of grain size, growth rate and properties of single-crystal monolayer WS_2 grown by CVD.

Substrate	Temperature	Time	Size	Growth Rate	Property	Reference
hBN flakes	900 ℃	10 min	3 μm	0.3 μm/min	-	1
Graphite	1100 ℃	15 - 30 min	15 μm	1.0 μm/min	-	2
SiO_2/Si	500 ℃	60 min	12.7 μm	0.2 μm/min	-	3
SiO_2/Si (ZnO)	1000 ℃	60 min	28.3 μm	0.5 μm/min	-	4
SiO_2/Si	880 - 780 ℃	40 min	52 μm	1.3 μm/min	-	5
SiO_2/Si (PTAS)	800 ℃	5 min	20 μm	4.0 μm/min	μ=0.01 $cm^2 V^{-1} s^{-1}$ ON/OFF=10^5	6
SiO_2/Si	860 ℃	60 min	370 μm	6.2 μm/min	-	7
SiO_2/Si	850 ℃	15 min	160 μm	10.7 μm/min	-	8
SiO_2/Si	1070 ℃	15 min	256 μm	17.1 μm/min	μ=2.2 $cm^2 V^{-1} s^{-1}$ ON/OFF=10^6	9
SiO_2/Si	900 ℃	10 min	250 μm	25.0 μm/min	μ=32.3 $cm^2 V^{-1} s^{-1}$ ON/OFF=10^6 (at 300 K)	10
SiO_2/Si	750 ℃	5 min	178 μm	35.6 μm/min	-	11
SiO_2/Si	825 ℃	-	200 μm	-	μ=14 $cm^2 V^{-1} s^{-1}$	12

SiO_2/Si Sapphire	850 - 950 °C	30 - 90 min	9.7 μm	0.3 μm/min	-	13
SiO_2/Si Sapphire	850 °C	15 min growth 10 min etch	>15 μm	~0.6 μm/min	-	14
Sapphire	900 °C	60 min	50 μm	0.8 μm/min	μ=0.46 cm^2 V^{-1} s^{-1} ON/OFF=10^2	15
Sapphire	900 °C	60 min	135 μm	2.3 μm/min	μ=4.1 cm^2 V^{-1} s^{-1} ON/OFF=10^5	16
Sapphire	950 °C	40 min	Centimeter scale film	-	μ=0.91 cm^2 V^{-1} s^{-1}; ON/OFF=10^6; R=18.8 mA/W (V_g=60 V,Vacuum); t< 4.5 ms(R=0.2 μA W^{-1}, Air)	17
Au foil	800 °C	240 min	600 μm	2.5 μm/min	μ=2 cm^2 V^{-1} s^{-1} ON/OFF=5×10^7	18
Au foil	935 °C	5 min 15 min	420 μm 600 mm^2	84.0 μm/min 40.0 mm^2/min	μ=20 cm^2 V^{-1} s^{-1} ON/OFF=10^8	19
Atomic sawtooth Au foil	800 °C	20 min	5×5 mm^2	1.3 mm^2/min	μ=3 cm^2 V^{-1} s^{-1} ON/OFF=10^8	20
SiO_2/Si	825 °C	45 min	4-in. film	0.09-in./min	μ=0.3 cm^2 V^{-1} s^{-1}	21

					ON/OFF=10^3	
SiO_2/Si	640-650 ℃	20 min	10 μm	0.5 μm/min	ON/OFF=10^4	22
SiO_2/Si	1000 ℃	-	200 μm	-	μ= 1.4 cm^2 V^{-1} s^{-1}	23
SiO_2	950 ℃	8 min	450 μm	56.25 μm/min	μ= 1.2 cm^2 V^{-1} s^{-1} ON/OFF=10^6	24
SiO_2/Si	825 ℃	15 min	-	-	μ= 0.1-1 cm^2 V^{-1} s^{-1} ON/OFF>10^6	25
Mica	860 ℃	-	~500 μm	30 μm/min	μ= 13.8 cm^2 V^{-1} s^{-1} ON/OFF=5.5×10^8	26
sapphire	980 ℃	40 min	2-inch film	49.1 mm^2/min	μ=0.02 cm^2 V^{-1} s^{-1} ON/OFF>5.5×10^3 t <560 μs R=0.52 mA W^{-1}	27
Sapphire	900 ℃	15 min	5mm film	-	R= 0.22 mA W^{-1}	28
SiO_2/Si	950 ℃	3 min	100 μm	33.33 μm/min	μ= 0.53 cm^2 V^{-1} s^{-1} ON/OFF= 10^6	29

Sapphire	950 °C	10-40 min	550 μm	13.75 μm/min	μ= 1.21 cm^2 V^{-1} s^{-1} R= 3.2 mA W^{-1}	30
SiO_2/Si	950 °C	30 min	150 μm	5 μm/min	μ= 8.1 cm^2 $V^{-1}s^{-1}$ ON/OFF= 10^5	31
Au foil	**850 ℃**	**36 min**	**520 μm**	**14.4 μm/min**	**μ=8.3 cm^2 $V^{-1}s^{-1}$ ON/OFF=10^3 R=22.9 mA W^{-1} t_{rise}=59 ms；t_{decay}=77 ms**	**This work**

Table S2. PL performance of reported TMDs.

Materials	**Synthetic Method**	**Treatment**	**Quantum Yield**		**Fluorescence Lifetime**		**Reference**
WS_2	Mechanical exfoliation	OA treatment	-		Before Fast decay =64 ps	After Fast decay =248 ps	32
WS_2	Mechanical exfoliation	-	-		0.195 ns		33
WS_2	Mechanical exfoliation	-	21±3 %		3.24±0.05 ns		34
MoS_2	Mechanical exfoliation	UV-TFSI treatment	-		Before 40 ps	After 1.35 ns	35
MoS_2	Mechanical	TFSI treatment	Before	After	Before	After	36

	exfoliation		1 %	95 %	100 ps	10.8 ± 0.6 ns	
MoS_2	Exfoliation	-	-		3 ns		37
MoS_2	Mechanical exfoliation	TFSI treatment	-		Before	After	38
					-	10.2 ns	
		varying V_g and the incident pump power	V_g=0V G = 6 × 10^{17} $cm^{-2} \cdot s^{-1}$	V_g= -20V G = 6 × 10^{15} $cm^{-2} \cdot s^{-1}$	V_g=0V	V_g= -20V	
			0.1 %	75±10%	-	6.9 ns	
MoS_2	CVD	TFMS treatment	Before	After	Before	After	39
			0.2 %	14.1 %	11 ps	50 ps	
WS_2			Before	After	Before	After	
			2.7 %	56.7 %	8 ps	36 ps	
WS_2	CVD	Oxygen incorporation	Before	After	Before	After	40
			-	9.3 %	21.6 ps	109.3 ps	
WS_2	CVD	-	-		2H Phase	3R Phase	41
					3.2 ns	1.1 ns	
WS_2	CVD （Spin-coated with Nafion）	applying a uniaxial strain	Before	After	-		42
			-	70%±10%			
WSe_2	CVD	SEMD process	Before	After	-		43
			3.1 %	60 %			
MoS_2	CVD	TFSI- treatment	Before	After	Before	After	44
			-	31±8 %	0.19 ns	4.2 ns	
WS_2	GE-MOCVD	-	-		Pristine	After	14

						Transfer	
					0.733 ns	1.15 ns	
WS_2	CVT	TFSI treatment	Before	After	Before	After	45
			20 %	over 95%	1.25 ns	3.4±0.3 ns	
WS_2	PVD	WO_3–WS_2 bilayer heterostructures	Before	After	Before	After	46
			0.1 %	11.6 %	25.7 ps	1397.8 ps	
WS_2	**AGE-CVD**	-	**1st G**	**5th G**	**1st G**	**5th G**	**This work**
			13.7 %	**52.6 %**	**1.8 ns**	**5.6 ns**	

References

[1] M. Okada, T. Sawazaki, K. Watanabe, T. Taniguch, H. Hibino, H. Shinohara, R. Kitaura, *ACS Nano* **2014**, *8*, 8273.

[2] Y. Kobayashi, S. Sasaki, S. Mori, H. Hibino, Z. Liu, K. Watanabe, T. Taniguchi, K. Suenaga, Y. Maniwa, Y. Miyata, *ACS Nano* **2015**, *9*, 4056.

[3] Z. Xu, Y. Lv, J. Li, F. Huang, P. Nie, S. Zhang, S. Zhao, S. Zhao, G. Wei, *RSC Adv.* **2019**, *9*, 29628.

[4] Z. Xu, Y. Lv, F. Huang, C. Zhao, S. Zhao, G. Wei, *Materials* **2019**, *12*, 1883.

[5] Q. Fu, W. Wang, L. Yang, J. Huang, J. Zhang, B. Xiang, *RSC Adv.* **2015**, *5*, 15795.

[6] Y.-H. Lee, L. Yu, H. Wang, W. Fang, X. Ling, Y. Shi, C.-T. Lin, J.-K. Huang, M.-T. Chang, C.-S. Chang, M. Dresselhaus, T. Palacios, L.-J. Li, J. Kong, *Nano Lett.* **2013**, *13*, 1852.

[7] Y. Rong, Y. Fan, A. L. Koh, A. W. Robertson, K. He, S. Wang, H. Tan, R. Sinclair, J. H. Warner, *Nanoscale* **2014**, *6*, 12096.

[8] S. Hu, X. Wang, L. Meng, X. Yan, *J. Mater. Sci.* **2017**, *52*, 7215.

[9] L. Dong, Y. Wang, J. Sun, C. Pan, Q. Zhang, L. Gu, B. Wan, C. Song, F. Pan, C. Wang, Z. Tang, J. Zhang, *2D Mater.* **2019**, *6*, 015007.

[10] Y. Yue, J. C. Chen, Y. Zhang, S. S. Ding, F. Zhao, Y. Wang, D. Zhang, R. J. Li, H. Dong, W. Hu, Y. Feng, W. Feng, *ACS Appl. Mater. Interfaces* **2018**, *10*, 22435.

[11] C. Cong, J. Shang, X. Wu, B. Cao, N. Peimyoo, C. Qiu, L. Sun, T. Yu, *Adv. Opt. Mater.* **2014**, *2*, 131.

[12] S. Li, S. Wang, D.-M. Tang, W. Zhao, H. Xu, L. Chu, Y. Bando, D. Golberg, G. Eda, *Appl. Mater. Today* **2015,** *1*, 60.

[13] L. Tang, T. Li, Y. Luo, S. Feng, Z. Cai, H. Zhang, B. Liu, H.-M. Cheng, *ACS Nano* **2020**, *14*, 4646.

[14] A. Cohen, A. Patsha, P. K. Mohapatra, M. Kazes, K. Ranganathan, L. Houben, D. Oron, A. Ismach, *ACS Nano* **2021**, *15*, 526.

[15] Y. Zhang, Y. Zhang, Q. Ji, J. Ju, H. Yuan, J. Shi, T. Gao, D. Ma, M. Liu, Y. Chen, X. Song, H. Y. Hwang, Y. Cui, Z. Liu, *ACS Nano* **2013**, *7*, 8963.

[16] Z.-Q. Xu, Y. Zhang, S. Lin, C. Zheng, Y. L. Zhong, X. Xia, Z. Li, P. J. Sophia, M. S. Fuhrer, Y.-B. Cheng, Q. Bao, *ACS Nano* **2015**, *9*, 6178.

[17] C. Lan, C. Li, Y. Yin, Y. Liu, *Nanoscale* **2015**, *7*, 5974.

[18] Y. Gao, Z. Liu, D.-M. Sun, L. Huang, L.-P. Ma, L.-C. Yin, T. Ma, Z. Zhang, X.-L. Ma, L.-M. Peng, H.-M. Cheng, W. Ren, *Nat. Commun.* **2015**, *6*, 8569.

[19] S. J. Yun, S. H. Chae, H. Kim, J. C. Park, J.-H. Park, G. H. Han, J. S. Lee, S. M. Kim, H. M. Oh, J. Seok, M. S. Jeong, K. K. Kim, Y. H. Lee, *ACS Nano* **2015**, *9*, 5510.

[20] S. H. Choi, H.-J. Kim, B. Song, Y. I. Kim, G. Han, H. T. T. Nguyen, H. Ko, S. Boandoh, J. H. Choi, C. S. Oh, H. J. Cho, J. W. Jin, Y. S. Won, B. H. Lee, S. J. Yun, B. G. Shin, H. Y. Jeong, Y.-M. Kim, Y.-K. Han, Y. H. Lee, S. M. Kim, K. K. Kim, *Adv Mater.* **2021**, *33*, 2006601.

[21] Z. Jia, J. Dong, L. Liu, J. Xiang, A. Nie, F. Wen, C. Mu, B. Wang, K. Zhai, Z. Yu, M. Kang and Z. Liu, *Appl. Phys. Lett.*, **2019**, 115, 163104.

[22] M. Okada, N. Okada, W. H. Chang, T. Endo, A. Ando, T. Shimizu, T. Kubo, Y. Miyata and T. Irisawa, *Sci Rep*, **2019**, 9, 17678.

[23] Z. Jia, W. Hu, J. Xiang, F. Wen, A. Nie, C. Mu, Z. Zhao, B. Xu, Y. Tian and Z. Liu, *Nanotechnology*, **2018**, 29, 255705.

[24] Z. Wang, H. Yang, S. Zhang, J. Wang, K. Cao, Y. Lu, W. Hou, S. Guo, X. A. Zhang and L. Wang, *Nanoscale*, **2019**, 11, 22440-22445.

[25] F. Zhang, Y. F. Lu, D. S. Schulman, T. Y. Zhang, K. Fujisawa, Z. Lin, Y. Lei, A. L. Elias, S. Das, S. B. Sinnott and M. Terrones, *Sci. Adv.*, **2019**, 5, 8.

[26] S. Zhou, L. Liu, S. Cui, X. Ping, D. Hu and L. Jiao, *Nano Res.*, **2020**, 14, 1659-1662.

[27] C. Y. Lan, Z. Y. Zhou, Z. F. Zhou, C. Li, L. Shu, L. F. Shen, D. P. Li, R. T. Dong, S. P. Yip and J. Ho, *Nano Res.*, **2018**, 11, 3371-3384.

[28] Z. Wan, Y. Wu, W. Yu, Y. Dong, Y. Huang and Q. Bao, *Phys. Status. Solidi. Rapid. Res. Lett.* **2019**, 13, 1900480.

[29] Y. Sheng, H. Tan, X. Wang and J. H. Warner, Chem. Mater., 2017, 29, 4904-4911.

[30]C. Lan, X. Kang, R. Wei, Y. Meng, S. Yip, H. Zhang and J. C. Ho, *ACS Appl. Mater. Interfaces*, **2019**, 11, 35238-35246.

[31] J. Chen, K. Shao, W. Yang, W. Tang, J. Zhou, Q. He, Y. Wu, C. Zhang, X. Li, X. Yang, Z. Wu and J. Kang, *ACS Appl. Mater. Interfaces,* **2019**, 11, 19381-19387.

[32] A. O. A. Tanoh, J. Alexander-Webber, J. Xiao, G. Delport, C. A. Williams, H. Bretscher, N. Gauriot, J. Allardice, R. Pandya, Y. Fan, Z. Li, S. Vignolini, S. D. Stranks, S. Hofmann, A. Rao, *Nano Lett.* **2019**, *19*, 6299.

[33] H. Liu, T. Wang, C. Wang, D. Liu, J. Luo, *J. Phys. Chem. C,* **2019**, *123*, 10087.

[34] S. E. Barker, S. Wang, R. H. Godiksen, G. W. Castellanos, M. Berghuis, T. V. Raziman, A. G. Curto, J. G. Rivas, *Adv. Opt. Mater.* **2019**, *7*, 1900351.

[35] Y. Yamada, K. Shinokita, Y. Okajima, S. N. Takeda, Y. Matsushita, K. Takei, T. Yoshimura, A. Ashida, N. Fujimura, K. Matsuda, D. Kiriya, *ACS Appl. Mater. Interfaces* **2020**, *12*, 36496.

[36] M. Amani, D.-H. Lien, D. Kiriya, J. Xiao, A. Azcatl, J. Noh, S. R. Madhvapathy, R. Addou, K. C. Santosh, M. Dubey, K. Cho, R. M. Wallace, S.-C. Lee, J.-H. He, J. W. Ager, X. Zhang, E. Yablonovitch, A. Javey, *Science* **2015**, *350*, 1065.

[37] Y. Xu, S. Chen, Z. Dou, Y. Ma, Y. Mi, W. Du, Y. Liu, J. Zhang, J. Chang, C. Liang, J. Zhou, H. Guo, P. Gao, X. Liu, Y. Che, Y. Zhang, *Mater. Horiz.* **2019**, *6*, 1416.

[38] D.-H. Lien, S. Z. Uddin, M. Yeh, M. Amani, H. Kim, J. W. Ager, E. Yablonovitch, A. Javey, *Science* **2019**, *364*, 468.

[39] Q. Feng, Y. Sun, Y. Li, J. Yan, W. Zhong, G. Yang, W. Liu, H. Xu, Y. Liu, *Laser Photonics Rev.* **2021,** *15*, 2100104.

[40] Q. Cui, Z. Luo, Q. Cui, W. Zhu, H. Shou, C. Wu, Z. Liu, Y. Lin, P. Zhang, S. Wei, H. Yang, S. Chen, A. Pan, L. Song, *Adv. Funct. Mater.* **2021**, *31*, 2105339.

[41] P. Kumar, N. C. Verma, N. Goyal, J. Biswas, S. Lodha, C. K. Nandi, V. Balakrishnan, *Nanoscale* **2018**, *10*, 3320.

[42] H. Kim, S. Z. Uddin, N. Higashitarumizu, E. Rabani, A. Javey, *Science* **2021,** *373*, 448.

[43] H. Kim, G. H. Ahn, J. Cho, M. Amani, J. P. Mastandrea, C. K. Groschner, D.-H. Lien, Y. B. Zhao, J. W. Ager, M. C. Scott, D. C. Chrzan, A. Javey, *Sci. Adv.* **2019**, *5*, eaau4728.

[44] M. Amani, R. A. Burke, X. Ji, P. Zhao, D.-H. Lien, P. Taheri, G. H. Ahn, D. Kirya, J. W. Ager, E. Yablonovitch, J. Kong, M. Dubey, A. Javey, *ACS Nano* **2016**, *10*, 6535.

[45] M. Amani, P. Taheri, R. Addou, G. H. Ahn, D. Kiriya, D.-H. Lien, J. W. Ager, R. M. Wallace, A. Javey, *Nano Lett.* **2016**, *16*, 2786.

[46] B. Zheng, W. Zheng, Y. Jiang, S. Chen, D. Li, C. Ma, X. Wang, W. Huang, X. Zhang, H. Liu, F. Jiang, L. Li, X. Zhuang, X. Wang, A. Pan, *J. Am. Chem. Soc.* **2019**, *141*, 11754.